Electronic Supplementary Information

Rationale for Highly Efficient and Outdoor-Stable Terpolymer Solar Cells

Hua Tang[1,6*], Zhihui Liao[2], Safakath Karuthedath[1,6+], Si Chen[1], Heng Liu[3], Jafar I Khan[1], Maxime Babics[1], Wenchao Yang[1], Maryam Alqurashi[1], Yakun He[1,4], Julien Gorenflot[1], Jiaming Huang[5], Gang Li[5], Stefaan De Wolf[1], Xinhui Lu[3], Christoph J. Brabec[4], Frédéric Laquai[1] and Shirong Lu [2*]

[1] KAUST Solar Center, Physical Sciences and Engineering Division (PSE), Materials Science and Engineering Program (MSE), King Abdullah University of Science and Technology (KAUST), Thuwal, 23955-6900, Kingdom of Saudi Arabia.

[2] Department of Material Science and Technology, Taizhou University, Taizhou 318000, P. R. China

[3] Department of Physics, The Chinese University of Hong Kong, New Territories, Hong Kong 999077, P. R. China.

[4] Institute of Materials for Electronics and Energy Technology (i-MEET), Friedrich-Alexander-Universität Erlangen-Nürnberg, Martensstrasse 7, 91058 Erlangen, Germany

[5] Department of Electronic and Information Engineering, The Hong Kong Polytechnic University, Hung Hum, Kowloon, Hong Kong SAR, P. R. China.

[6] H.T, and S.K contributed equally to this work.

[+] Present address: Institute of Materials Research, Tsinghua Shenzhen International Graduate School, Tsinghua University, Shenzhen, 518055 China

Corresponding authors.

E-mail: H., Tang hua.tang.1@kaust.edu.sa, S., Lu lushirong@tzc.edu.cn,

Content

1. Materials

D18, PM6, Y6, and PNDIT-F3N in this work were purchased from Solarmer Material Inc. The D18-based terpolymers, including (D18(5%TZ), D18(10%TZ), and D18(50%TZ)) and PM6-based terpolymers, including (PM6(5%TZ), PM6(10%TZ), and PM6(50%TZ)) were synthesized by Z. L,. The chloroform (CF), acetone, isopropanol, methanol, and ethanoic acid were purchased from Sigma-Aldrich.
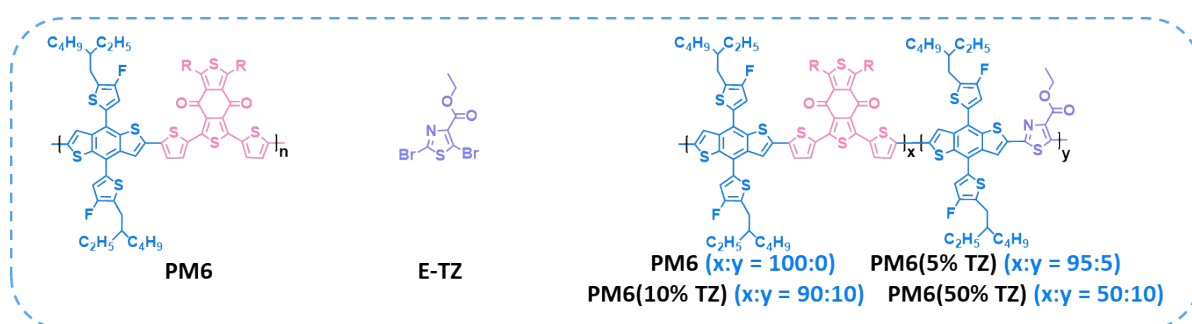

Figure S1. Molecular structures of PM6, E-TZ, PM6(5% TZ), PM6(10% TZ), and PM6(50% TZ).

2. Device Fabrication

The organic solar cells were prepared on glass substrates with tin-doped indium oxide (ITO, 15 Ω/sq) patterned on the surface (device area: 0.1 cm^2). Substrates were prewashed with isopropanol to remove organic residues before immersing in an ultrasonic bath of soap for 15 min. Samples were rinsed in flowing deionized water for 5 min before being sonicated for 30 min each in successive baths of deionized water, acetone and isopropanol. Then, the samples were dried with pressurized nitrogen before being exposed to a UV-ozone plasma for 20 min.

A thin layer (ca. 30 nm) of PEDOT:PSS (Bayer Baytron 4083) was first spin-coated on the substrates with 4000 rpm and baked at 150 °C for 10 min under ambient conditions. The substrates were then transferred into a nitrogen-filled glove box. The active layer solution of D18:Y6, D18(5%TZ):Y6, D18(10%TZ):Y6, and D18(50%TZ):Y6 devices was obtained by dissolving D18 or D18-based terpolymers and Y6 in chloroform (CF) employing a D/A ratio of 1:1.2 with donor concentration of ~ 5.2 mg/ml. The mixed solution was stirred for at least 3

h under 100 °C, and then cooled down to 50 °C and stirred for 10 min before spin-coating. Active layer are spun at 1800 rpm (the film thickness ~ 135 nm) and then solvent annealing with CF for 30 s. Then, a ~10 nm-thin layer of PNDIT-F3N (0.5 mg ml^{-1}, 0.5% ethanoic acid, methanol) was coated on top as electron transport layer. The samples were then dried at room temperature for 1 hour. Finally, the samples were placed in a thermal evaporator for evaporation of a 100 nm-thick layer of Silver (Ag) evaporated at 0.1 Å s^{-1} for the first 10 nm and 2 Å s^{-1} for the next 90 nm; pressure of less than 2x10^{-6} Torr.

The current density-voltage (J-V) curves of devices were measured using a Keithley 2400 Source Meter in glove box under AM 1.5G (100 mW cm^{-2}) using a Enlitech solar simulator (purchased from Enli Technology Co., Ltd.). A 2×2 cm^2 monocrystalline silicon reference cell with KG5 filter (purchased from Enli Tech. Co., Ltd., Taiwan). The external quantum efficiency (EQE) was measured by a certified incident photon to electron conversion (IPCE) equipment (QE-R) from Enli Technology Co., Lt. The light intensity at each wavelength was calibrated using a standard monocrystalline Si photovoltaic cell.

3. The Status of Terpolymer photovoltaics

Table S1. Summary of the state-of-the-art terpolymer photovoltaics in recent years.

Terpolymerization	Donor	Acceptor	V_{OC} [V]	J_{SC} [mA cm^{-2}]	FF [%]	Max (Ave) PCE [%]	ref
N	PBDB-TT0 (0% D2)		0.886	11.75	69.93	7.28 (7.16)	
Y	PBDB-TT5 (5% D2)	PC$_{71}$BM	0.853	14.04	70.37	8.42(8.34)	
Y	PBDB-TT10 (10% D2)		0.836	13.90	66.79	7.76(7.59)	
Y	PBDB-TT20 (20% D2)		0.803	13.78	62.04	6.86(6.67)	[1]
N	PBDB-TT0 (0% D2)		0.930	16.27	60.04	9.08 (8.98)	
Y	PBDB-TT5 (5% D2)	m-ITIC	0.913	17.53	69.79	11.17 (11.10)	
Y	PBDB-TT10 (10% D2)		0.900	17.06	58.54	8.99 (8.87)	
Y	PBDB-TT20 (20% D2)		0.885	16.81	54.38	8.09 (7.90)	
N	Pt0 (0% A2)		0.80	25.10	64.9	13.03 (12.60)	
Y	Pt5 (5% A2)	Y6	0.80	25.89	72.7	15.06 (14.66)	[2]
Y	Pt10 (10% A2)		0.81	26.45	76.3	16.35 (16.02)	
Y	Pt15 (15% A2)		0.82	26.02	73.9	15.77 (15.41)	
N	PM6 (0% A2)		0.839	25.011	73.4	15.41 (14.74)	
Y	S1 (20% A2)	Y6	0.877	25.402	73.7	16.42 (15.75)	[3]
Y	S2 (50% A2)		0.896	22.954	63.6	13.08 (12.78)	

Y	S3 (80% A2)		0.911	19.915	50.2	9.11 (8.71)	
Y	S4 (100% A2)		0.929	12.777	48.5	5.76 (5.55)	
N	PM6-lr0 (0% A2)		0.835	25.60	71.98	15.39 (15.24)	
Y	PM6-lr0.5 (0.5% A2)		0.845	26.28	74.02	16.44 (16.32)	
Y	PM6-lr1 (1% A2)	Y6	0.845	26.15	78.40	17.32 (17.12)	[4]
Y	PM6-lr2.5 (2.5% A2)		0.847	26.07	74.15	16.37 (16.18)	
Y	PM6-lr5 (5% A2)		0.842	25.92	73.43	16.03 (15.88)	
N	PM6 (0% A2)		0.86	25.5	72	15.8 (15.6)	
Y	PM1 (20% A2)	Y6	0.87	25.9	78	17.6 (17.3)	[5]
Y	PM2 (50% A2)		0.90	24.9	69	15.5 (15.2)	
N	PM6 (0% A2)		0.85	25.6	72	15.7 (15.5)	
Y	PM6-Tz20 (20% A2)	Y6	0.85	26.3	77	17.1 (16.9)	[6]
Y	PM6-Tz40 (40% A2)		0.85	25.3	72	15.5 (15.3)	
N	PM6 (0% A2)	Y6-C2	0.840	25.65	73.01	15.73 (15.42)	[7]
Y	PM6-Ir1.5 (1.5% A2)		0.839	26.09	77.98	17.09 (16.80)	
N	PM6 (0% A2)		0.842	25.18	72.67	15.41 (15.29)	
Y	PM6-SiCl-10% (10% A2)	Y6	0.870	25.37	73.48	16.22 (16.11)	[8]
Y	PM6-SiCl-15% (15% A2)		0.875	25.26	70.03	15.48 (15.36)	
Y	PM6-SiCl-15% (20% A2)		0.881	24.88	67.24	14.73 (14.59)	
N	PM6 (0% A2)	N3	0.838	25.21	71.72	15.15 (14.91)	[9]

Y	PM6-5Si (5% A2)		0.852	26.32	75.81	17.01 (16.71)
Y	PM6-10Si (10% A2)		0.833	24.48	72.87	14.86 (14.60)
Y	PM6-15Si (15% A2)		0.829	23.98	69.07	13.74 (13.48)

4. Photo-Electron Spectroscopy in Air (PESA)

Photoelectron spectroscopy in air (PESA) measurements were performed employing a Riken Keiki PESA spectrometer (Model AC-2) with a power setting of 10 nW and a power number of 0.33. Thin film samples for PESA were prepared on glass substrates.
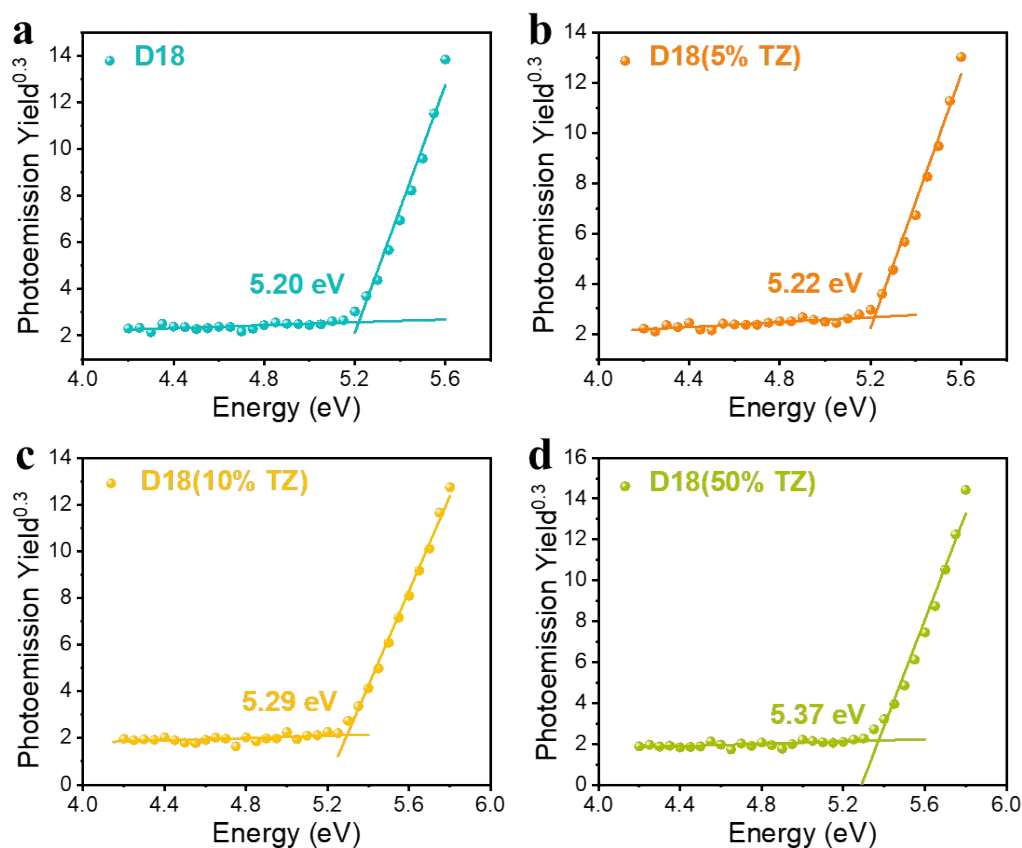

Figure S2. PESA data of neat D18, D18(5% TZ), D18(10% TZ), and D18(50% TZ) films used in this study. The highest occupied molecular orbital (HOMO) levels of the corresponding materials are obtained by fitting the PESA results (solid line).
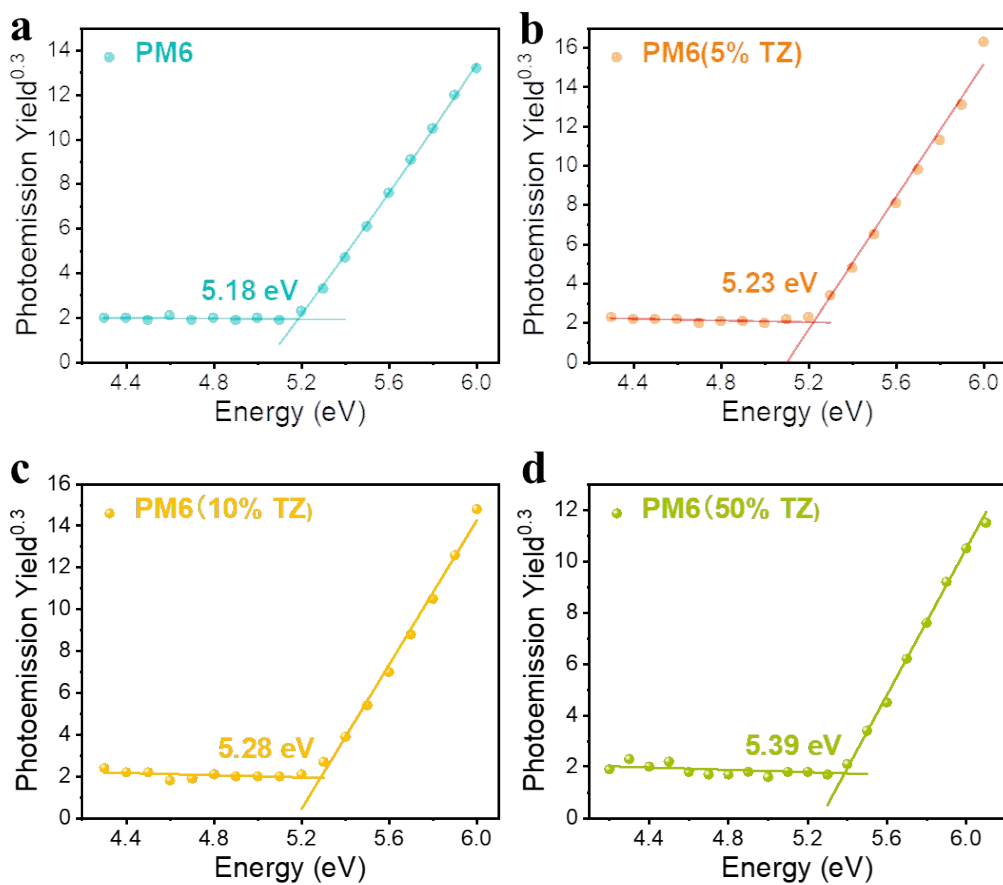
Figure S3. PESA data of neat PM6, PM6(5% TZ), PM6(10% TZ), and PM6(50% TZ) films used in this study. The HOMO levels of the corresponding materials are obtained by fitting the PESA results (solid line).

5. Optical Bandgap

The optical bandgap is obtained from intersection of absorption and PL emission spectra.
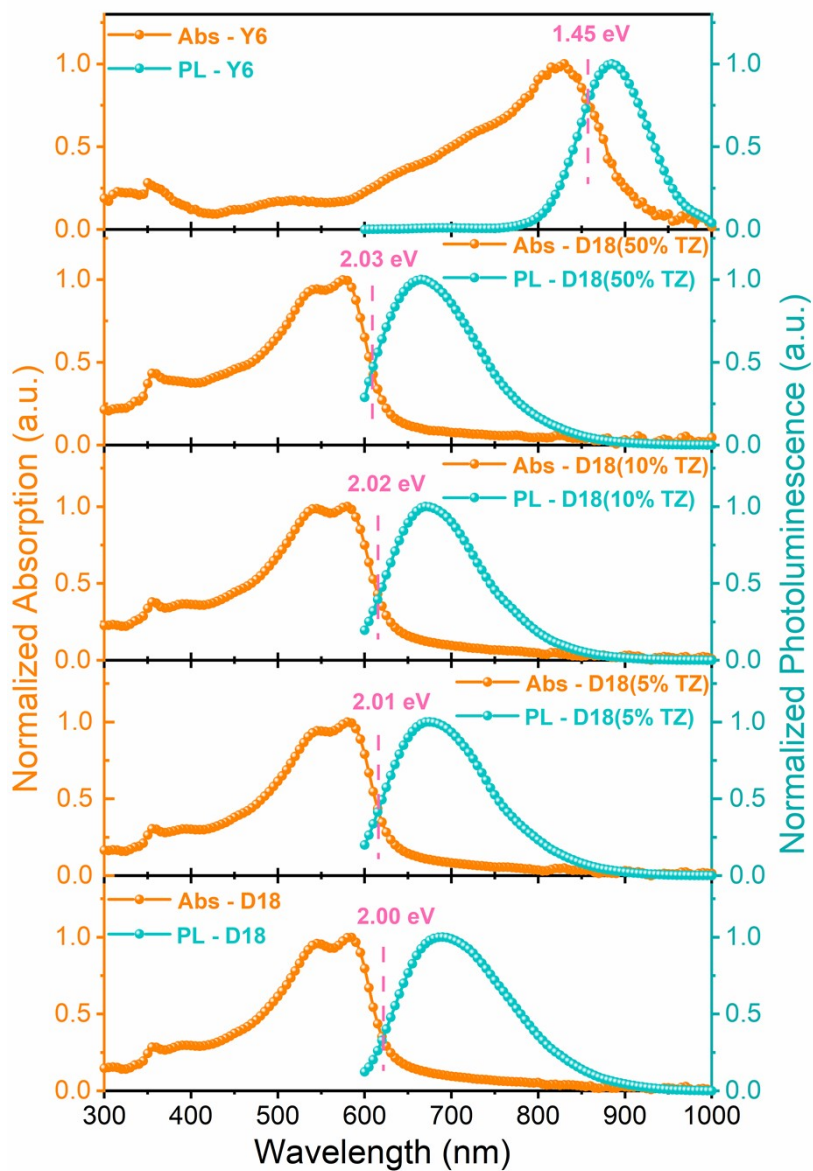

Figure S4. UV-vis absorption and photoluminescence (PL) emission spectra of D18, D18(5%TZ), D18(10%TZ), D18(50%TZ), and Y6 neat films, respectively.
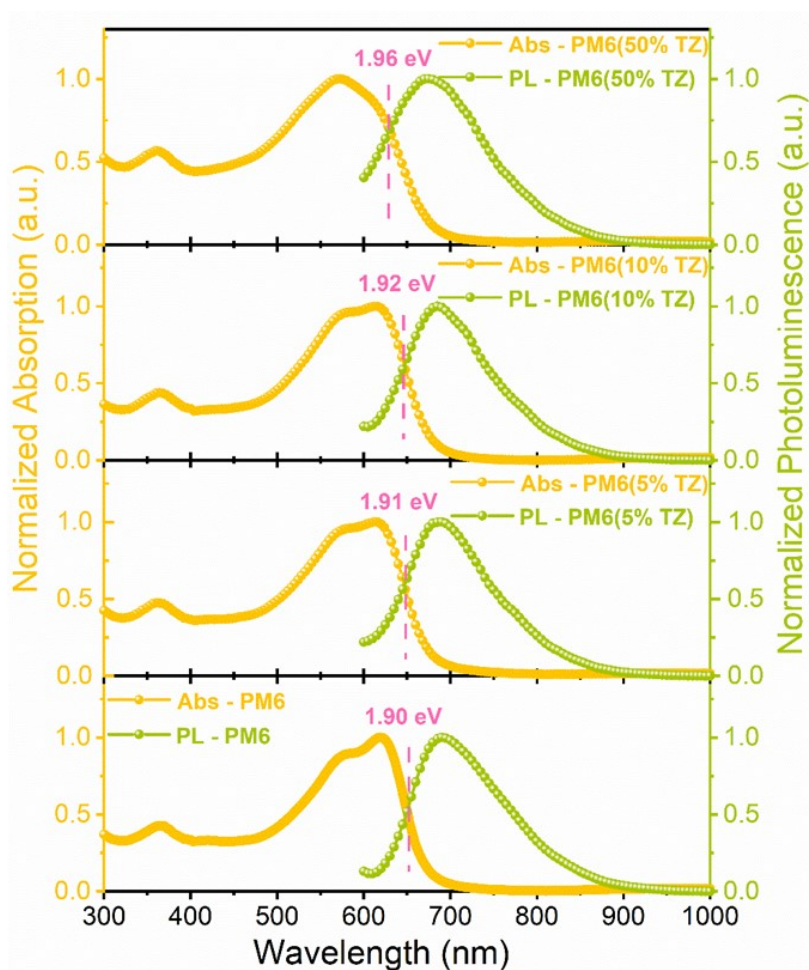
Figure S5. UV-vis absorption and photoluminescence (PL) emission spectra of PM6, PM6(5%TZ), PM6(10%TZ), and PM6(50%TZ) neat films, respectively.
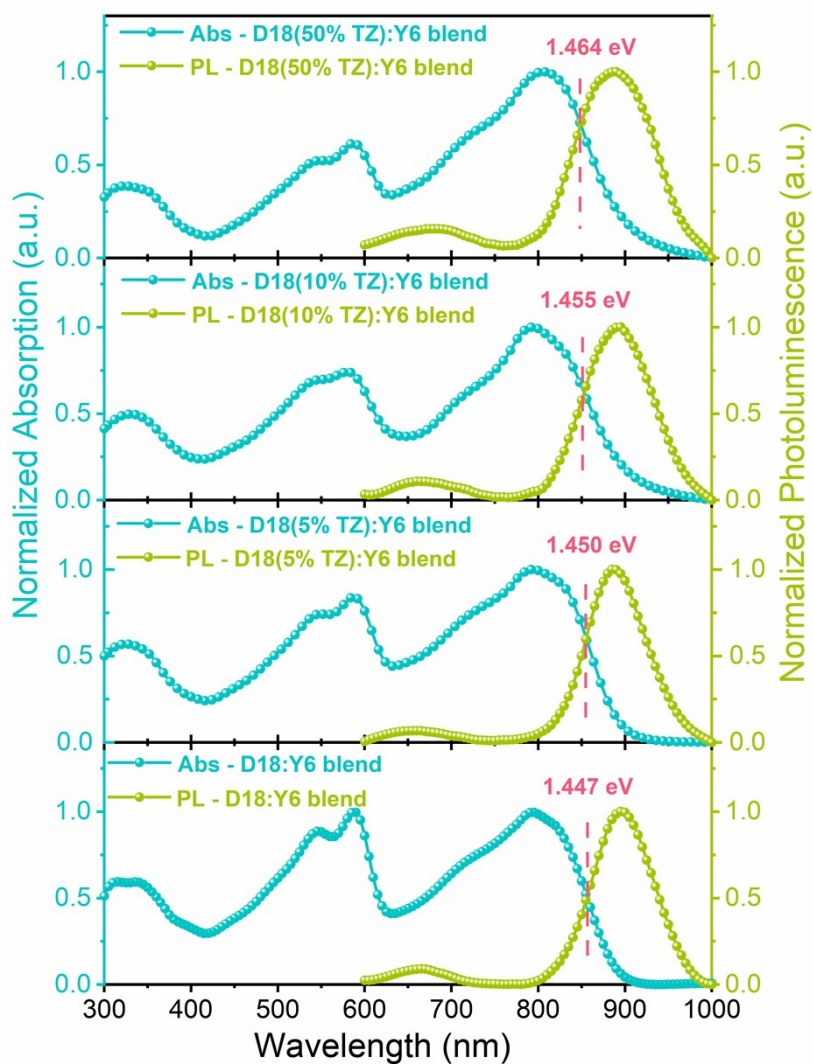
Figure S6. UV-vis absorption and photoluminescence (PL) emission spectra of D18:Y6, D18(5%TZ):Y6, D18(10%TZ):Y6, and D18(50%TZ):Y6 blend films, respectively.

6. Energy Levels Diagram

The lowest unoccupied molecular orbital (LUMO) levels were calculated based on HOMO levels obtained from PESA and optical bandgaps obtained from intersection of absorption and PL emission spectra of the corresponding materials,
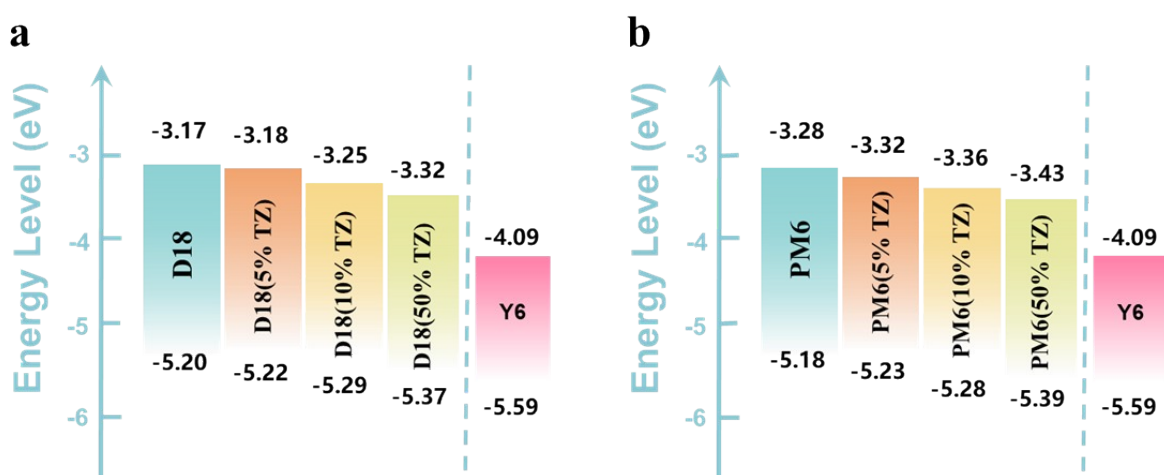

Figure S7. Energy level diagrams of **a** D18, D18(5%TZ), D18(10%TZ), and D18(50%TZ) and **b** PM6, PM6(5%TZ), PM6(10%TZ), PM6(50%TZ), and Y6.

7. GIWAXS/GISAXS

GIWAXS/GISAXS measurements were carried out with a Xeuss 2.0 SAXS/WAXS laboratory beamline using a Cu X-ray source (8.05 keV, 1.54 Å) and a Pilatus3R 300K detector. The incidence angle is 0.2°.

Silicon substrates for GIWAXS/GISAXS test were sonicated for 20 min each in successive baths of detergent, DI water, acetone and isopropanol. The substrates were then dried with pressurized nitrogen before being exposed to the UV−ozone for 20 min. The active layers were prepared following the methods described in Section of Device Fabrication.
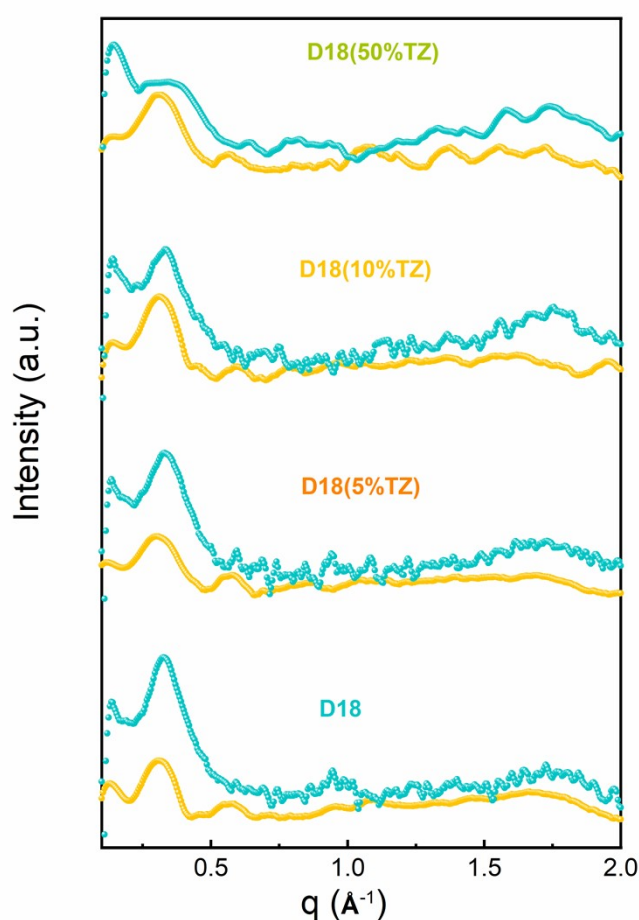

Figure S8. Corresponding GIWAXS intensity profiles along the out-of-plane (OOP) and in-plane (IP) directions of D18, D18(5%TZ), D18(10%TZ), and D18(50%TZ) neat films.

Table S2. Detailed GIWAXS line-cut information of D18, D18(5%TZ), D18(10%TZ), and D18(50%TZ) neat films.

Component	Peak	Peak location ($Å^{-1}$)	FWHM ($Å^{-1}$)	Crystal coherence length(nm)
D18	(100)OOP	0.33	0.085	6.65
	(010)OOP	1.75	0.207	2.73
D18(5%TZ)	(100)OOP	0.33	0.092	6.14
	(010)OOP	1.73	1.731	2.28
D18(10%TZ)	(100)OOP	0.33	0.107	5.28
	(010)OOP	1.73	0.289	1.96
D18(50%TZ)	(100)OOP	0.33	0.281	2.01
	(010)OOP	1.73	0.357	1.58

Table S3. Detailed GIWAXS peak information along the IP and OOP directions of D18:Y6, D18(5%TZ):Y6, D18(10%TZ):Y6, and D18(50%TZ):Y6 blend films.

Component	Peak	Peak location (Å^{-1})	FWHM (Å^{-1})	Crystal coherence length(nm)
D18:Y6	(100)IP	0.312	0.107	5.28
	(010)OOP	1.801	0.214	2.64
D18(5%TZ):Y6	(100)IP	0.313	0.121	4.67
	(010)OOP	1.765	0.222	2.55
D18(10%TZ):Y6	(100)IP	0.306	0.133	4.25
	(010)OOP	1.778	0.239	2.36
D18(50%TZ):Y6	(100)IP	0.295	0.143	3.95
	(010)OOP	1.764	0.247	2.29

Table S4. The calculated results for XDAB which refer to intermixing D/A domain size and 2Rg representing the phase with larger short-distance crystallinity that is dominated by Y6 of D18:Y6, D18(5%TZ):Y6, D18(10%TZ):Y6, and D18(50%TZ):Y6 blend films.

Component	X_{DAB} (nm)	$2R_g$ (nm)
D18:Y6	27	19
D18(5%TZ):Y6	25	20
D18(10%TZ):Y6	25	12
D18(50%TZ):Y6	24	13

8. Time-resolved photoluminescence (TRPL)

The TR-PL samples were excited with the wavelength-tunable Chameleon Ultra Laser (Coherent, central wavelength 820 nm) at 450 and 725 nm. The fundamental of the Chameleon is pumping a Radiantis OPO, from which the generated second harmonic 450 nm (fundamental 900 nm) is used to excite the samples. The repetition rate of the fs pulses was 80 MHz, and typical pulse energies were in the range of 500 nJ. The PL of the samples was collected by an optical telescope (consisting of two plano-convex lenses) and focused on the slit of a spectrograph (PI Spectra Pro SP2300) and detected with a Streak Camera (Hamamatsu C10910) system with a temporal resolution of 1.4 ps. The data was acquired in photon counting mode using the Streak Camera software (HPDTA) and exported to Origin Pro 2020 for further analysis.
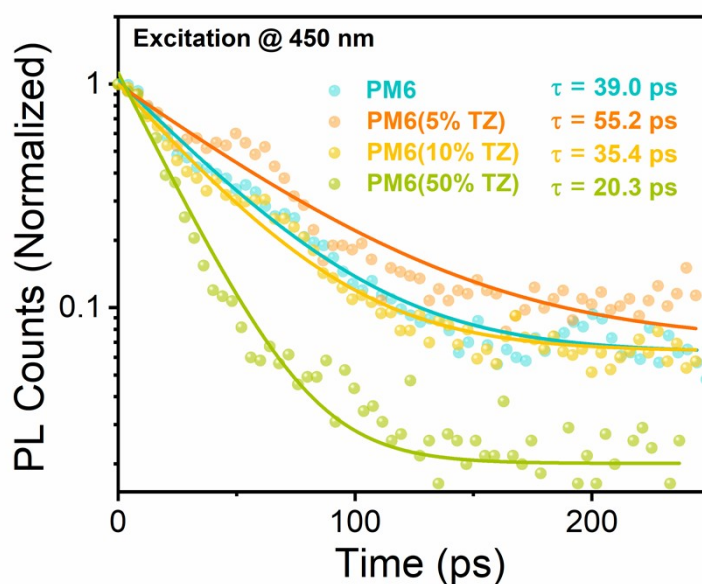

Figure S9. TRPL measurements following optical excitation at 450 nm for **a** PM6, **b** PM6(5%TZ), **c** PM6(10%TZ), and **d** PM6(50%TZ) neat film.

9. Estimation of the improvement of exciton diffusion lengths

It is observed that for the mono-exponential fitting of the TRPL decay kinetics, the fitting curves always lie above the actual signal in the initial short time range, suggesting the presence of possible exciton-exciton annihilation (EEA) process, which can make the exciton decay more rapidly. As such we tried to fit the TRPL kinetics in the short time range of below 100 ps using the EEA equation[10] (1), where $n(n_0)$ is the exciton (initial) density, τ is the lifetime obtained by the mono-exponential fitting to the whole time range using equation (2), and γ is the EEA coefficient.

$$\frac{n}{n_0} = \frac{e^{-t/\tau}}{1 + \gamma n_0 \tau (1 - e^{-t/\tau})} \qquad (1)$$

$$\frac{n}{n_0} = e^{-t/\tau} \qquad (2)$$

The product $\gamma n_0 \tau$ in the denominator of equation (1) is dimensionless and can be obtained by the best fitting to the TRPL kinetics below 100 ps. The EEA fitting can help us gain some insights into the exciton diffusion lengths in terpolymer donor with different percentages of TZ. According to the EEA theory,

$$\gamma = 4\pi RD \quad , \qquad (3)$$

where R is the EEA capture radius and assumed to be the same for the different acceptors. The exciton diffusion length

$$L_D = \sqrt{D\tau} = \sqrt{\gamma \tau / 4\pi R} \quad . \quad (4)$$

We assume that the photo-excited initial exciton density n_0 are approximately the same given that the EQEs do not show much difference among the four donors. Then the ratio of L_D for any of the two donors satisfy

$$\frac{L_{D1}}{L_{D2}} = \sqrt{\frac{\gamma_1 \tau_1 n_0}{\gamma_2 \tau_2 n_0}} = \sqrt{\frac{c_1}{c_2}} \quad , \qquad (5)$$

In which $c = \gamma n_0 \tau$ is the dimensionless fitting parameter to be obtained. In **Figure S10a** the EEA fittings for the TRPL kinetics are shown. The lifetimes τ used in the fitting and the extracted fitting parameter c's are as presented in Table S1. It is clear that the EEA fitting give a good description of the rapid decay behavior of TRPL kinetics in the intial time range of 0-100 ps, while the monoexponetial fitting for the whole time range shown in Figure **S10b** fails to acount

for the behavior, suggesting the presence of EEA process in the initial time regime. The obtained c's are substituted into equation (5) to estimate the ratios between the exciton diffusion lengths. It is found that with respect to the L_D in D18, the exciton diffusion lengths in 5%TZ, 10%TZ and 50%TZ are 1.1^{L_D}, 0.8^{L_D} and 0.8^{L_D}, respectively. Therefore, under the EEA scenario, the enhanced lifetime in 5%TZ exhibits the largest exciton diffusion length. The L_D for 5%TZ is improved by a factor of at least 1.1 relative to that of D18.
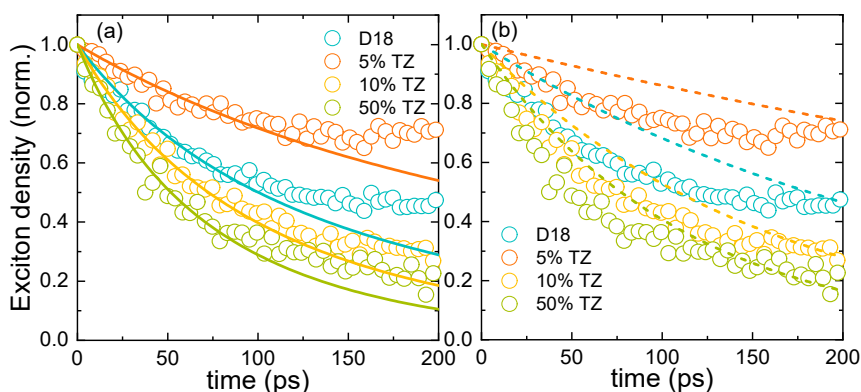

Fig. S10. The EEA fitting (a) and the mono-exponential fitting (b) for the experimental TRPL kinetics in the time range of 0-100 ps for the 4 donors. Obviously the EEA fitting can reproduce the initial TRPL kinetics much more closely, suggesting the presence of EEA process in this time regime.

Table S5. The exciton lifetime τ used in the EEA fitting by equation (1), which is extracted from the monoexponential fitting to the exciton dynamics in the entire time range, the $c\,(\gamma n_0 \tau)$ obtained by the EEA fitting to the first 100 ps exciton decay dynamics, and the ratio of exciton diffusion lengths (L_D) relative to that of D18 (L_{D0}) estimated by equation (5) for each donor.

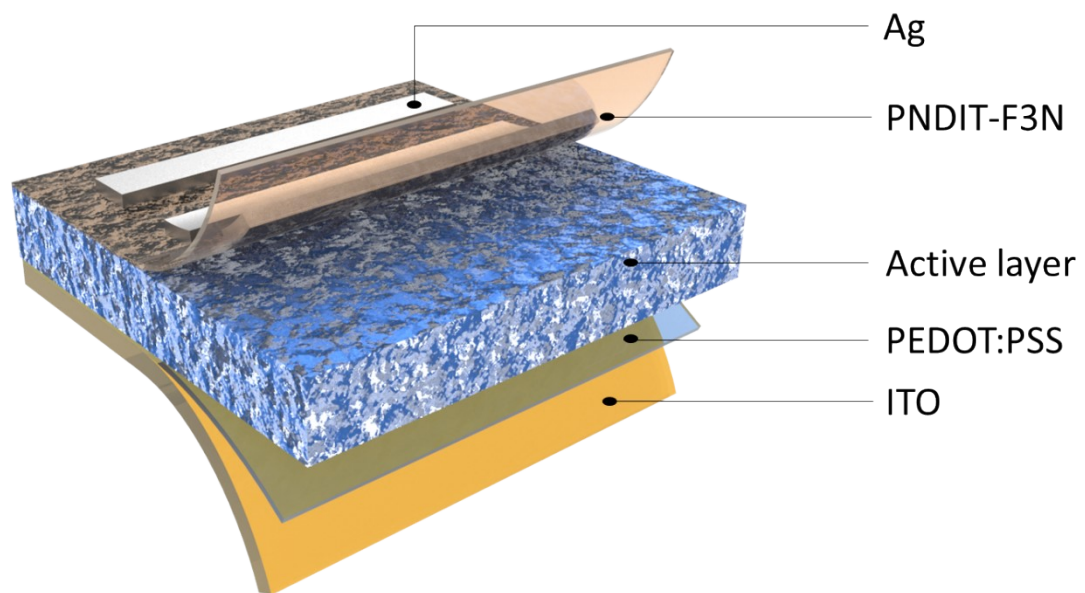| Donors	τ (ps)	$c\,(\gamma n_0 \tau)$	L_D/L_{D0}
D18	234	0.889 ± 0.054	1
D18(5%TZ)	566	1.045 ± 0.062	1.1
D18(10%TZ)	149	0.591 ± 0.039	0.8
D18(50%TZ)	109	0.634 ± 0.056	0.8

10. Device Architecture

Figure S11. The device architecture used in this work.

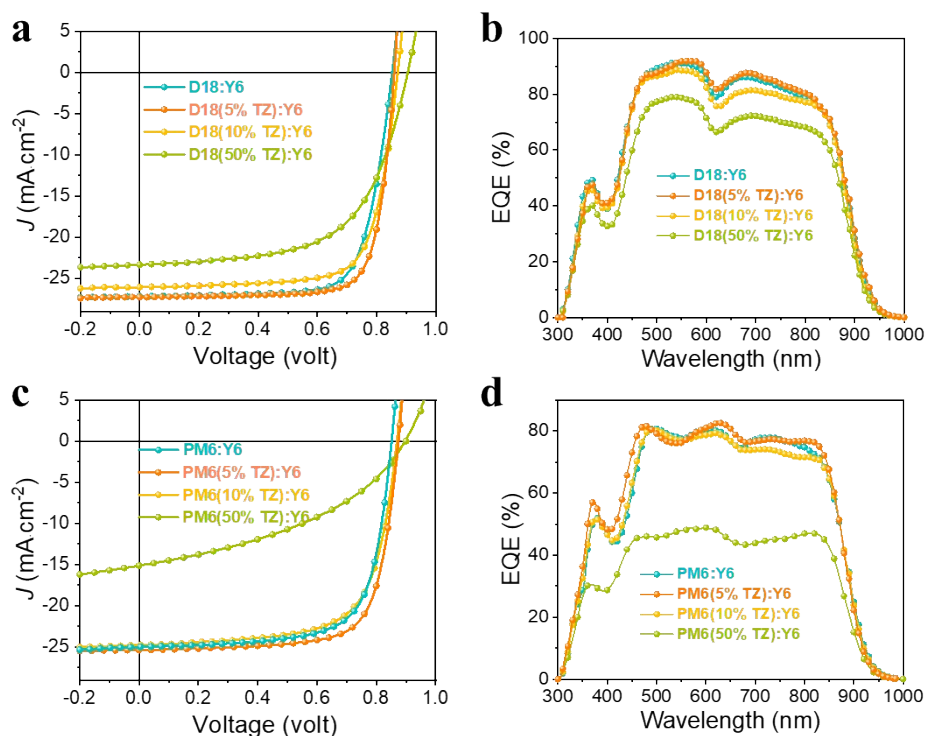# 11. Photovoltaic Performance of Terpolymer Photovoltaics

Figure S12. a *J*-V and **b** EQE of D18:Y6, D18(5%TZ):Y6, D18(10%TZ):Y6, and D18(50%TZ):Y6 devices. **c** *J*-V and **d** EQE of PM6:Y6, PM6(5%TZ):Y6, PM6(10%TZ):Y6, and PM6(50%TZ):Y6 devices.

Table S6. Summary of photovoltaic performance of PM6:Y6, PM6(5%TZ):Y6, PM6(10%TZ):Y6, and PM6(50%TZ):Y6 devices under simulated AM1.5G illumination (100 mW cm^{-2}).

Active layer	V_{OC} [V]	J_{SC} [mA cm^{-2}]	J_{EQE} [mA cm^{-2}]	FF [%]	PCE [%]
PM6:Y6	0.839	25.1	24.5	72.8	15.4
PM6(5%TZ):Y6	0.871	25.3	24.8	73.7	16.3
PM6(10%TZ):Y6	0.871	24.8	24.0	67.1	14.5
PM6(50%TZ):Y6	0.900	15.1	14.7	40.7	5.5

12. CT states and energy loss calculations

The following equations have been applied to calculate the voltage losses:

rEL = reduced electroluminescence intensity

f_1 and f_2 = relative amplitude coefficients

λ = reorganization energy associated with the CT process

k = Boltzmann constant

T = absolute temperature

E_g = optical energy gap

J_{SC} = short-circuit current density

q = elementary charge

$J_{0,rad}$ = saturation current density at radiative limit

E_{CT} = charge-transfer state energy

ϕ_{BB} = the black body radiation

$$rEL_{blend}(E) = f_1 rEL_{acceptor}(E) + \frac{f_2}{\sqrt{4\pi\lambda kT}} e^{\frac{(E_{CT}-\lambda-E)^2}{4\lambda kT}} \qquad (5)$$

$$\Delta E_{CT} = E_g - E_{CT} \qquad (6)$$

$$\Delta V_{OC, rad} = \frac{kT}{q} ln(\frac{J_{SC}}{J_{0,rad}} + 1) \qquad (7)$$

$$J_{0,rad} = q \int_0^\infty EQE_{PV}(E)\phi_{BB}(E)dE \qquad (8)$$

$$q\Delta V_{OC,rad} = E_g - \Delta E_{CT} - q\Delta V_{OC,nonrad} \qquad (9)$$

$$q\Delta V_{OC,nonrad} = \frac{kT}{q} ln(\frac{J_{SC}}{J_{0,rad}} + 1) - V_{OC} \qquad (10)$$

13. Transient Absorption (TA) Spectroscopy

TA spectroscopy was carried out on blend films using a homebuilt pump–probe setup. Two different configurations of the setup were used for either short delay, namely from 100 fs to 8 ns experiments, or long delay, namely from 1 ns to 300 μs delays, as described in the following.

The output of a titanium:sapphire amplifier (Coherent LEGEND DUO, 4.5 mJ, 3 kHz, 100 fs) was split into three beams (2, 1, and 1.5 mJ). Two of them were used to separately pump two optical parametric amplifiers (OPA) (Light Conversion TOPAS Prime). TOPAS 1 generates tunable pump pulses, , while TOPAS 2 generates signal (1300 nm) and idler (2000 nm) only. . For short delay TA measurements, TOPAS 1 was used to generate 600 nm pump pulses, while the probe pathway length to the sample was kept constant at ≈ 5 m between the output of TOPAS 1 and the sample. The pump pathway length was varied between 5.12 and 2.6 m with a broadband retroreflector mounted on an automated mechanical delay stage (Newport linear stage IMS600CCHA controlled by a Newport XPS motion controller), thereby generating delays between pump and probe from ~ 400 ps to 8 ns.

For the 1 ns to 300 μs delay (long delay) TA measurement, the same probe white-light supercontinuum was used as for the 100 fs to 8 ns delays. Here the excitation light (pump pulse) was provided by an actively Q-switched Nd:YVO4 laser (InnoLas picolo AOT) frequency doubled to provide pulses at 532 and 355 nm. The pump laser was triggered by an electronic delay generator (Stanford Research Systems DG535) itself triggered by the transistor–transistor logic (TTL) sync from the Legend DUO, allowing control of the delay between pump and probe with a jitter of roughly 100 ps.

Pump and probe beams were focused on the sample which was kept under a dynamic vacuum of <10−5 mbar. The transmitted fraction of the white light was guided to a custom-made prism spectrograph (Entwicklungsbüro Stresing), where it was dispersed by a prism onto a 512 pixel complementary metal-oxide semiconductor (CMOS) linear image sensor (Hamamatsu G11608-512DA). The probe pulse repetition rate was 3 kHz, while the excitation pulses were mechanically chopped to 1.5 kHz (100 fs to 8 ns delays) or directly generated at 1.5 kHz frequency (1 ns to 300 µs delays), while the detector array was read out at 3 kHz. Adjacent diode readings corresponding to the transmission of the sample after excitation and in the absence of an excitation pulse were used to calculate ΔT/T. Measurements were averaged over several thousand shots to obtain a good signal-to-noise ratio. The chirp induced by the transmissive optics was corrected with a homebuilt Matlab code. The delay at which pump and probe arrive simultaneously on the sample (i.e., zero time) was determined from the point of maximum positive slope of the TA signal rise for each wavelength.
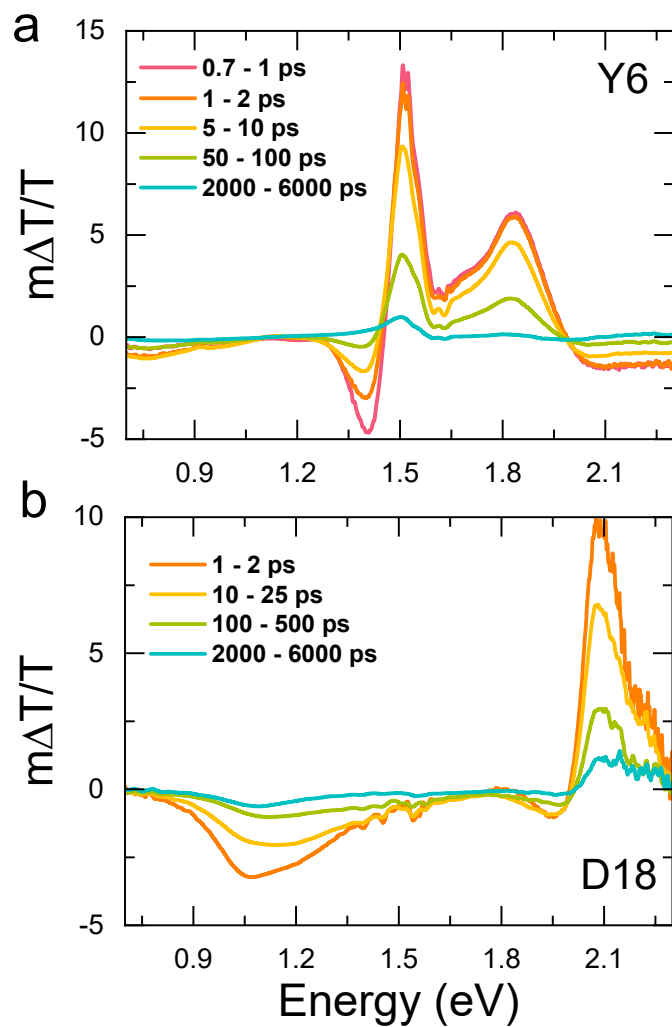
Figure S13: ps-ns TA spectra of **a** neat Y6 and **b** neat D18 films after exciting at 650 nm.
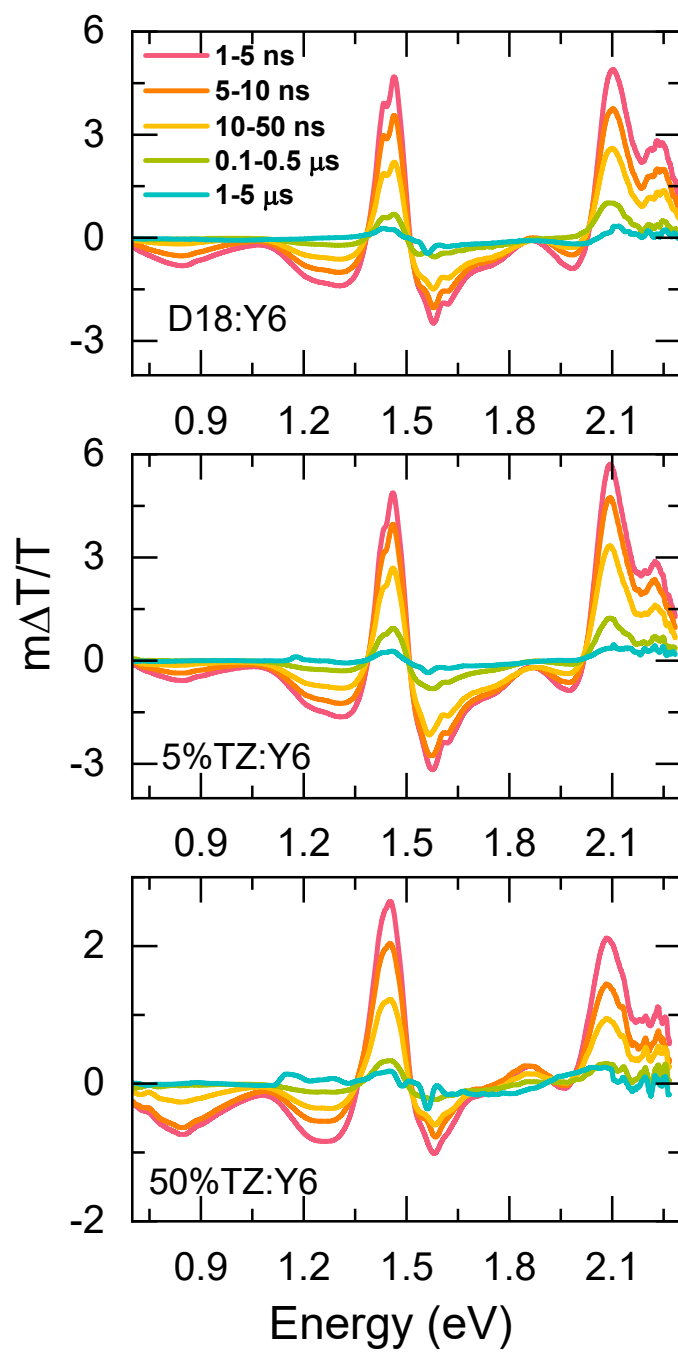
Figure S14: ns-us TA spectra of D18:Y6 (a), D18-5%TZ:Y6 (b), and D18-50%TZ:Y6 (c) blend film after exciting at 532 nm.

14. Effective bimolecular recombination coefficient

The two-pool model is based on concomitant fluence-independent geminate recombination of charge-transfer states charge carriers (CT-carriers) and fluence-dependent non-geminate recombination of spatially separated free charges. Assuming that charges in CT-states and spatially-separated (free) charges have similar photo-induced absorption features and thus cannot be spectroscopically distinguished, the dynamics of the entire charge carrier population can be described by Equation 1:[11]

$$n(t) = (N_0(1-f)\left[\exp\left(-k_{CT \to GS}t\right)\right] + [\lambda \gamma t + (fN_0)^{-\lambda}]^{\frac{-1}{\lambda}}) \qquad (S1)$$

Here, $k_{CT \to GS}$ is the monomolecular (geminate) recombination rate constant, $\lambda+1$ and γ are the apparent non-geminate recombination order and coefficient, respectively, and f is the fraction of the initial carrier population that decays non-geminately (equivalent to the fraction of separated charges). $n(t)$ is the time-dependent carrier population undergoing recombination. N_0 is the total initial charge carrier density, which was estimated by assuming an absorption cross-section on the order of 1×10^{-16} cm^2 for charge carriers and from the $\Delta T/T$ signal amplitude of the PA band at 10 ns delay time by using the Beer-Lambert formula:

$$\Delta T/T = \sigma(\lambda)\ N\_0\ d \qquad (S2)$$

$$N_0 = \frac{\frac{\Delta T}{T}}{\sigma(\lambda)\ d} \qquad (S3)$$

where $\frac{\Delta T}{T}$ is the TA signal amplitude at a specific fluence, d is the thickness of the film and $\sigma(\lambda)$ is the absorption cross-section of charge carriers. We note that we fit the carrier decay dynamics globally, that is, by using a set of shared parameters and across all measured fluences. Further details of this model can be in our earlier works.[11-13]

Empirically the non-geminate recombination of separated charges is found to follow an apparent order $\lambda+1$ higher than two:

	$\dfrac{dn}{dt} = -\gamma\, n^{\lambda+1}$		(S4)

Which can also be written as a bimolecular recombination with a *n-dependent* recombination coefficient β:

$$\frac{dn}{dt} = -\beta\, n^2 \qquad\qquad \text{(S5)}$$

With $\beta = \gamma\, n^{\lambda - 1}$

Several theories currently exist to explain this dependence such as field dependent mobility, immobilization (trapping) of a part of the charges,[14] non-uniform distribution of the charges through the layer thickness,[15] or equilibrium between separated charges and interfacial CT-state.[16]

Reason for mismatch of β values obtained from TA and TDCF

We note that for both samples the non-geminate recombination coefficients obtained by TA and TDCF differ quite substantially. This mismatch is largely due to the n-dependence of β: indeed in TA, non geminate recombination is found to exhibit an order of λ+1, the equivalent β_{TA} is thus calculated as $\beta_{TA} = \gamma.n^{\lambda-1}$ (by equalizing the theoretical and experimental recombination rates: $\beta_{TA}.n^2 = \gamma.n^{\lambda+1}$). The value presented in Table 2 (in the main draft) corresponds to the value that β_{TA} takes for a charge density of 1×10^{16} cm^{-3} considered as representative of a device under operation. We relate the mismatch to the fact that β_{TDCF} is obtained by fitting the evolution of number of charges extracted when applying the collection field (V_{col}), this implicitly considers that all the charges having escaped the device before V_{col} is applied have recombined. This does not make a difference for short delays due to the prebias applied -- close to V_{OC} -- that limits the current until applying the extraction field; however, when integrated over larger delays this current still leads to the leakage of a rather large density of charges before the application of V_{OC}, considering those charges as having recombined thus leads to an over-estimation of the recombination coefficient. But clearly at higher carrier densities, larger recombination coefficients are obtained. Detailed explanation can be found in one of our previous works.[17]

15. Time Delayed Collection Field (TDCF)

The home-built TDCF setup used the second harmonic (532 nm) of an actively Q-switched sub-ns Nd:YVO4laser (INNOLAS picolo AOT) operating at 5 kHz as excitation. To minimize the RC response time (typically few nanoseconds), a small device area of 1 mm² was used. The samples were measured under dynamic vacuum conditions to avoid any degradation. A Keysight S1160A functional generator was used to provide the pre-bias and extraction bias, while a Keysight four channel digital oscilloscope was used to measure the current response of the device.
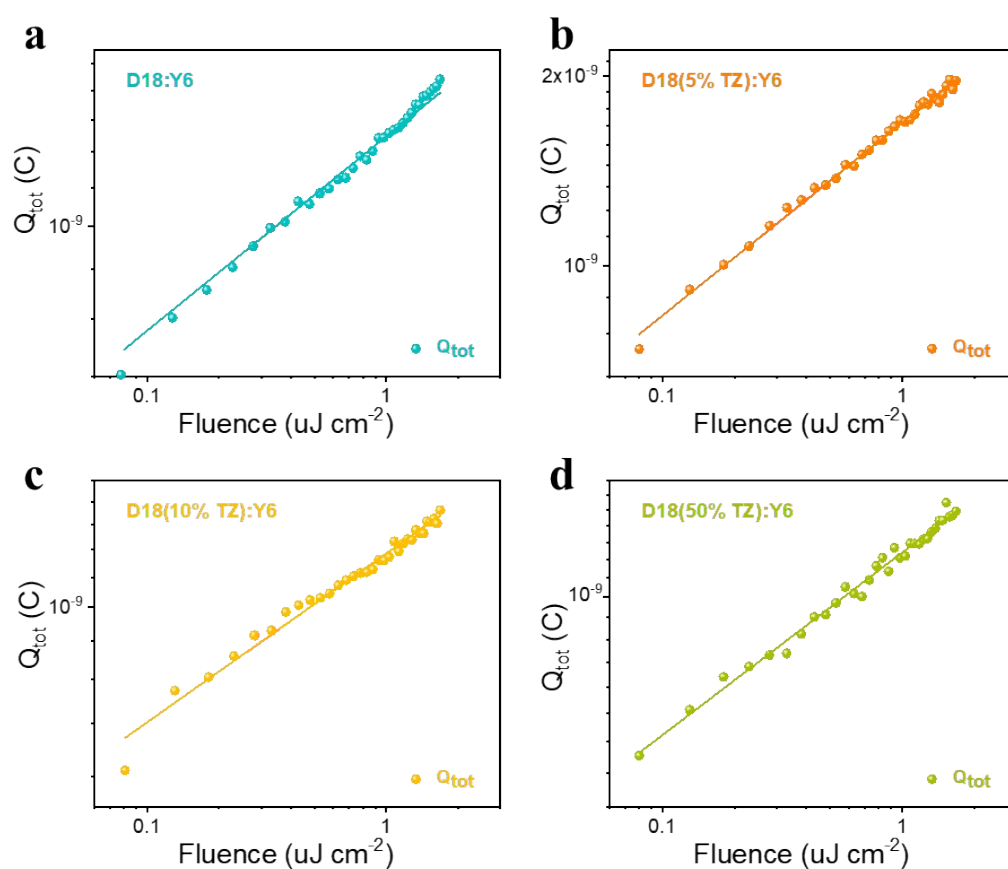

Figure S15. TDCF measurements on **a** D18:Y6, **b** D18(5%TZ):Y6, **c** D18(10%TZ):Y6, and **d** D18(50%TZ):Y6 devices: the total charge (Q_{tot}) plotted against the excitation laser fluence. The experimental data are shown as dots, whilst the solid line indicates the linear response regime of Q_{tot} vs. pump fluence.
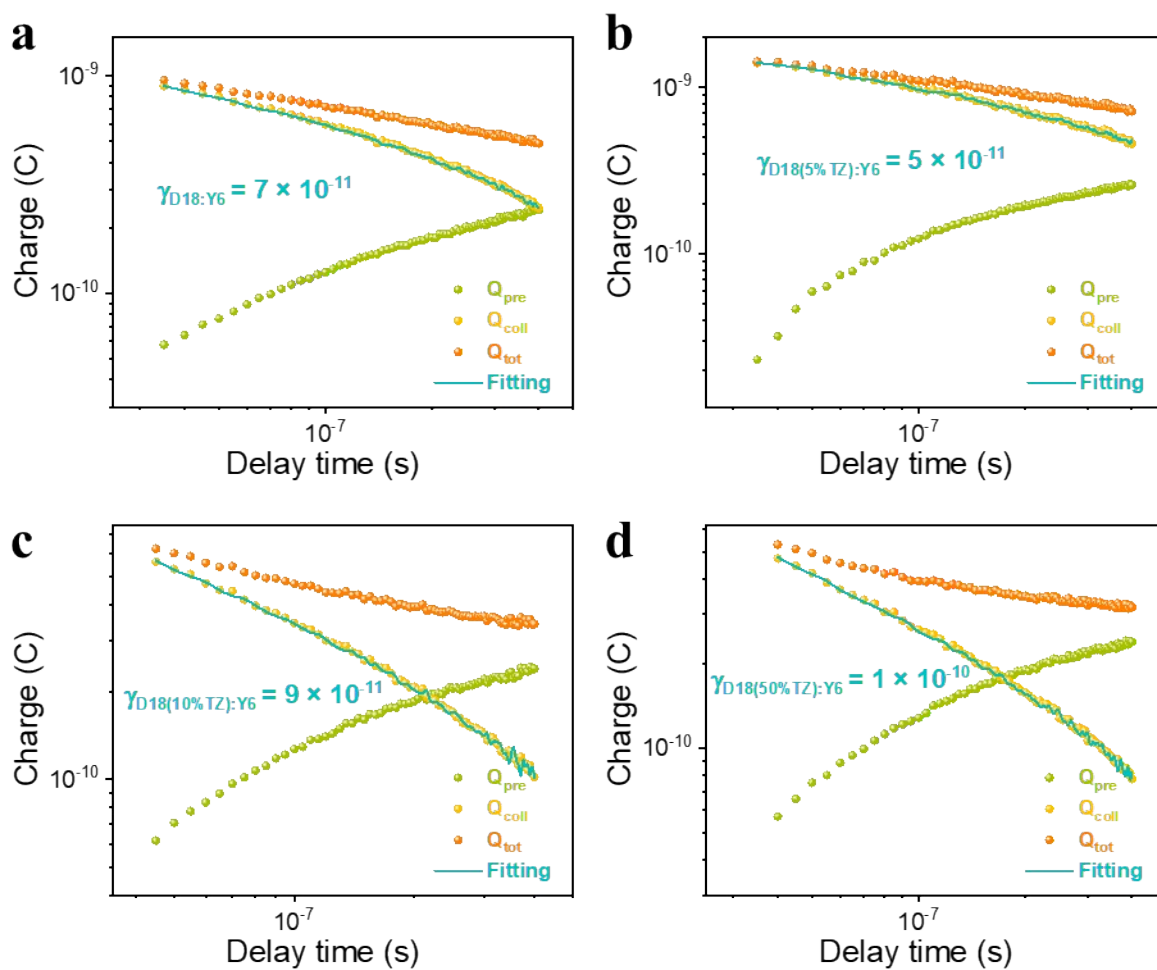
Figure S16. Plots of $Q_{pre}(t_d)$, $Q_{col}(t_d)$, and $Q_{tot}(t_d)$ as determined from TDCF transients recorded for a prebias near V_{OC} as a function of delay time (t_d) for **a** D18:Y6, **b** D18(5%TZ):Y6, **c** D18(10%TZ):Y6, and **d** D18(50%TZ):Y6 devices.

16. SCLC Measurements

Fitting the hole/electron-only diode dark current to the space charge limited current (SCLC) model can obtain the hole and electron mobility of the photoactive layer. The electron-only device structure was ITO/ZnO/ PNDIT-F3N/ BHJ/ PNDIT-F3N /Ag, and the hole-only device structure was ITO/PEDOT:PSS/BHJ/MoO$_3$/Ag. Using the following equation to estimate the electric-field dependent SCLC mobility:

$$J(V) = \frac{9}{8}\varepsilon_0\varepsilon_r\mu_0 exp\left(0.89\beta\sqrt{\frac{V - V_{bi}}{L}}\right)\frac{(V - V_{bi})^2}{L^3}$$

For the hole-only device structure, V$_{bi}$ = 0 V (flat band pattern formed by PEDOT:PSS-MoO$_3$); For the electron-only device structure, V$_{bi}$ = 0.5V was used following the protocol reported.[18, 19]
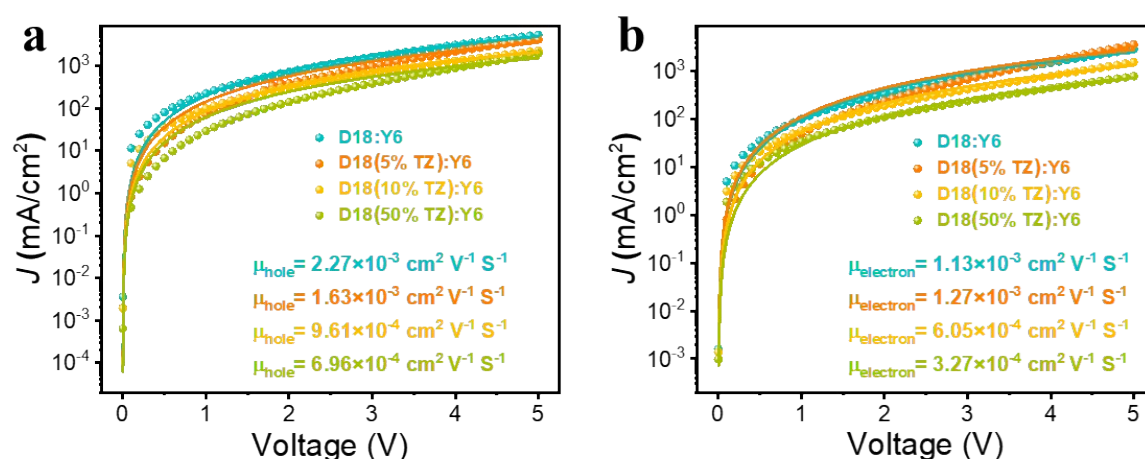

Figure S17. Dark J–V curves of the BHJ and BHJ(DPO) OSCs: (a) electron-only diodes and (b) hole-only diodes; The solid lines are fit to the experimental data according to the above equation.

Table S7. Summary of carrier mobilities

Active layer	μ_h [$\times 10^{-4}$ cm^2 V^{-1} s^{-1}]	μ_e [$\times 10^{-3}$ cm^2 V^{-1} s^{-1}]	μ_h / μ_e
D18:Y6	2.27×10^{-3}	1.13×10^{-3}	2.01
D18(5%TZ):Y6	1.63×10^{-3}	1.27×10^{-3}	1.28
D18(10%TZ):Y6	9.61×10^{-4}	6.05×10^{-4}	1.59
D18(50%TZ):Y6	6.96×10^{-4}	3.27×10^{-4}	2.13

17. Numerical Device Simulator

The 1D numerical drift-diffusion device simulator (Setfos 5.2 from FLUXiM AG) was used to simulate the device J–V characteristics of D18-based terpolymer photovoltaics. Optical constants (refractive index n and extinction coefficient k) of all layers were determined by variable angle spectroscopic ellipsometry (VASE) with an M-2000 ellipsometer (J.A. Woolam Co., Inc).
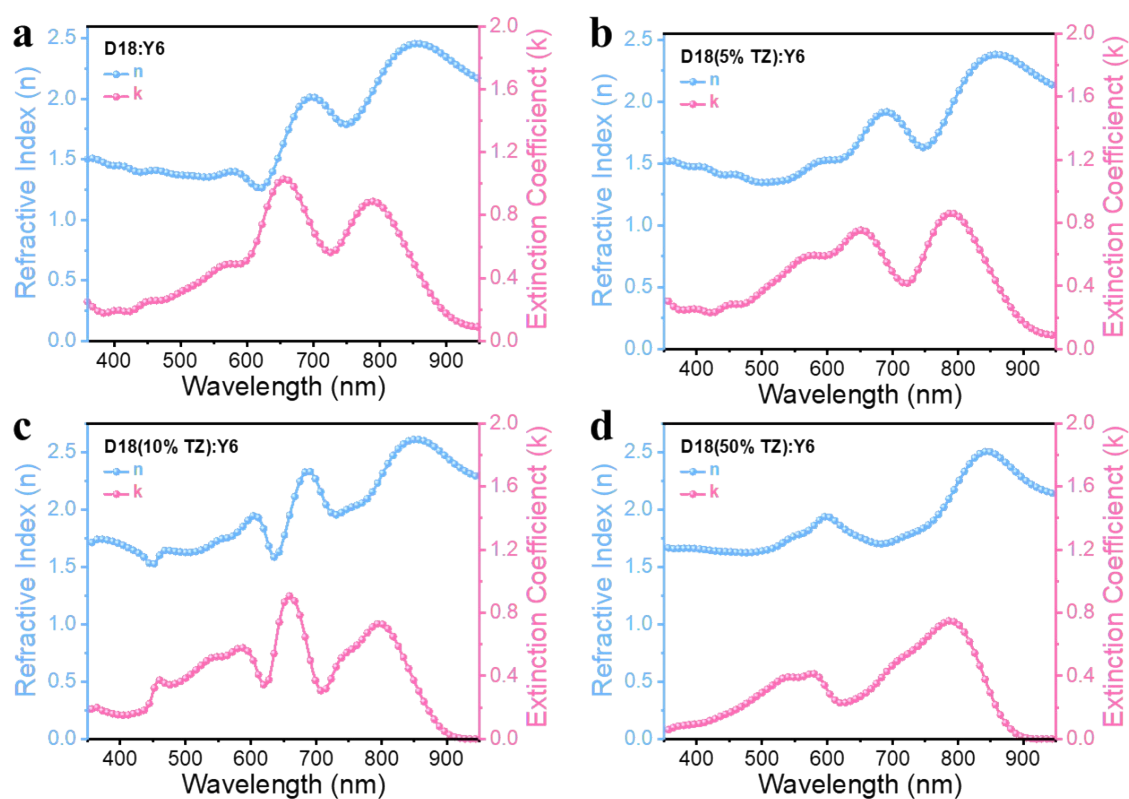

Figure S18. The n and k values fitted from the ellipsometry measurements of **a** D18:Y6, **b** D18(5%TZ):Y6, **c** D18(10%TZ):Y6, and **d** D18(50%TZ):Y6 blend films.
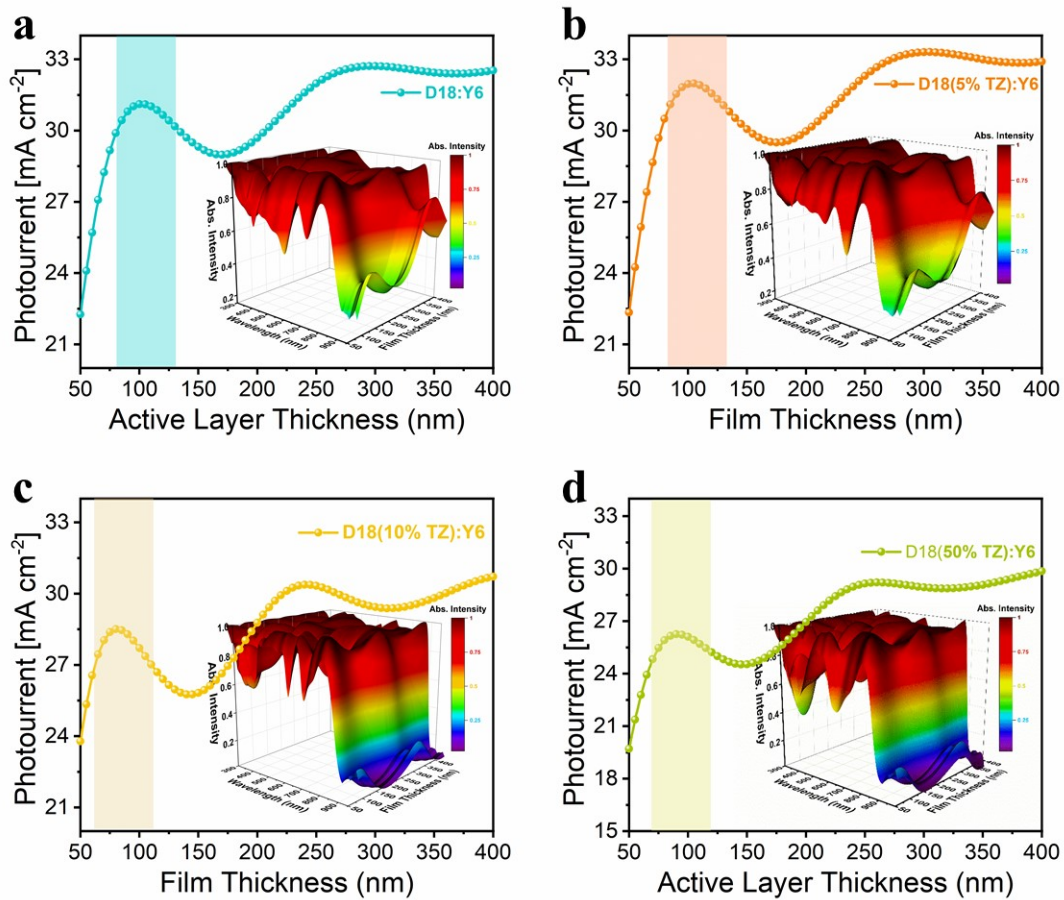
Figure S19. Simulated photocurrent as a function of active layer thickness **a** D18:Y6, **b** D18(5%TZ):Y6, **c** D18(10%TZ):Y6, and **d** D18(50%TZ):Y6 devices.

Table S8. Simulated figures of merit of devices.

D18:Y6	V_{OC} (V)	J_{SC} (mA cm^{-2})	FF (%)	PCE (%)
Simulation (β_{TDCF})	0.853	27.18	74.2	17.2
Simulation ($\beta \approx 10^{-12}$ cm^3 s^{-1})	0.878	27.26	77.8	18.6
D18(5% TZ):Y6	V_{OC} (V)	J_{SC} (mA cm^{-2})	FF (%)	PCE (%)
Simulation (β_{TDCF})	0.863	27.37	77.3	18.3
Simulation ($\beta \approx 10^{-12}$ cm^3 s^{-1})	0.884	27.41	78.4	19.0
D18(10% TZ):Y6	V_{OC} (V)	J_{SC} (mA cm^{-2})	FF (%)	PCE (%)
Simulation (β_{TDCF})	0.872	26.10	71.2	16.2
Simulation ($\beta \approx 10^{-12}$ cm^3 s^{-1})	0.899	26.20	76.2	17.9
D18(50% TZ):Y6	V_{OC} (V)	J_{SC} (mA cm^{-2})	FF (%)	PCE (%)
Simulation (β_{TDCF})	0.905	23.50	62.4	13.3
Simulation ($\beta \approx 10^{-12}$ cm^3 s^{-1})	0.935	23.74	71.3	15.8

18. Contact Angle Measurement

Table S9. Summarized Contact Angles and Surface Energy Parameters of D18, D18(5%TZ), D18(10%TZ), D18(50%TZ), and Y6 neat films.

films	Contact Angle (deg) [a) H_2O]	[b) formamide,FA]	Average Contact Angle (deg) [a) H_2O]	[b) formamide,FA]	surface energy γ (mJ m^{-2})
D18	93.2	82.3			
	92.1	82.8			
	92.5	83.5	93.22	82.48	18.58
	94.1	82.1			
	94.2	81.7			
D18(5% TZ)	98.5	83.3			
	99.3	83.1			
	99.5	82.6	99.10	83.12	19.13
	98.1	82.8			
	100.1	83.8			
D18(10% TZ)	96.7	79.6			
	98.3	79.8			
	97.8	78.8	97.12	78.74	22.38
	95.3	77.9			
	97.5	77.6			
D18(50% TZ)	97.6	77.9			
	96.8	76.7			
	96.5	75.9	96.96	76.46	24.70
	97	76.1			
	96.9	75.7			
Y6	92	73.5			
	91.7	72.7			
	91.7	73	91.70	72.68	25.83
	92	72			
	91.1	72.2			

a) Deionized water; b) formamide.

The contact angles of the films were performed on a DSA-100 (KRUSS Germany) contact angle meter. Then the surface free energy was calculated by Owens-Wendt method:[20, 21]

$$\gamma_L \times (1 + \cos\theta) = 2 \times \left(\gamma_L^d \cdot \gamma_{sv}^d\right)^{1/2} + 2 \times \left(\gamma_L^p \cdot \gamma_{sv}^p\right)^{1/2}$$

where γ_L and γ_s are surface free energy of the probe liquid and sample, respectively, θ is the contact angle of the sample.

The average contact angles of two liquids (deionized water and formamide) on the various neat films were measured and the results (Test 5 times separately) in **Table S3**, and the average contact angles and surface energy parameters are summarized in **Table S3**. Then calculate the Flory-Huggins interaction parameter $\chi_{donor-acceptor}$ for blend to show the binary miscibility from
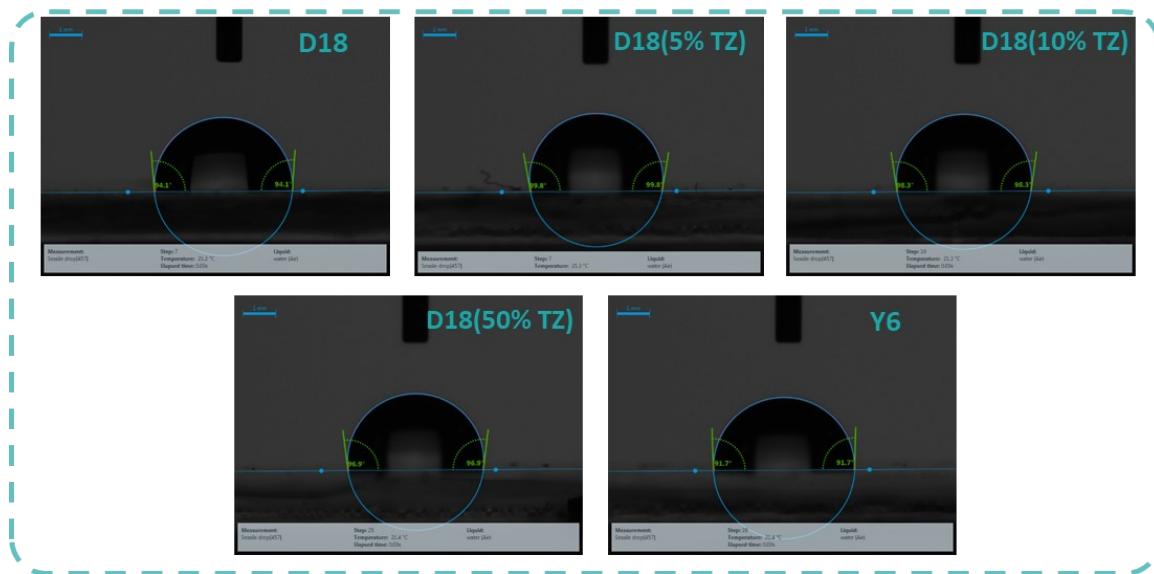
$$K\left(\gamma_{donor}^{1/2} - \gamma_{acceptor}^{1/2}\right)^2$$

where γ is the surface energy of the material, K is the proportionality constant. [22, 23]

Table S10. The miscibility of D18:Y6, D18(5%TZ):Y6, D18(10%TZ):Y6, and D18(50%TZ):Y6 blend films.

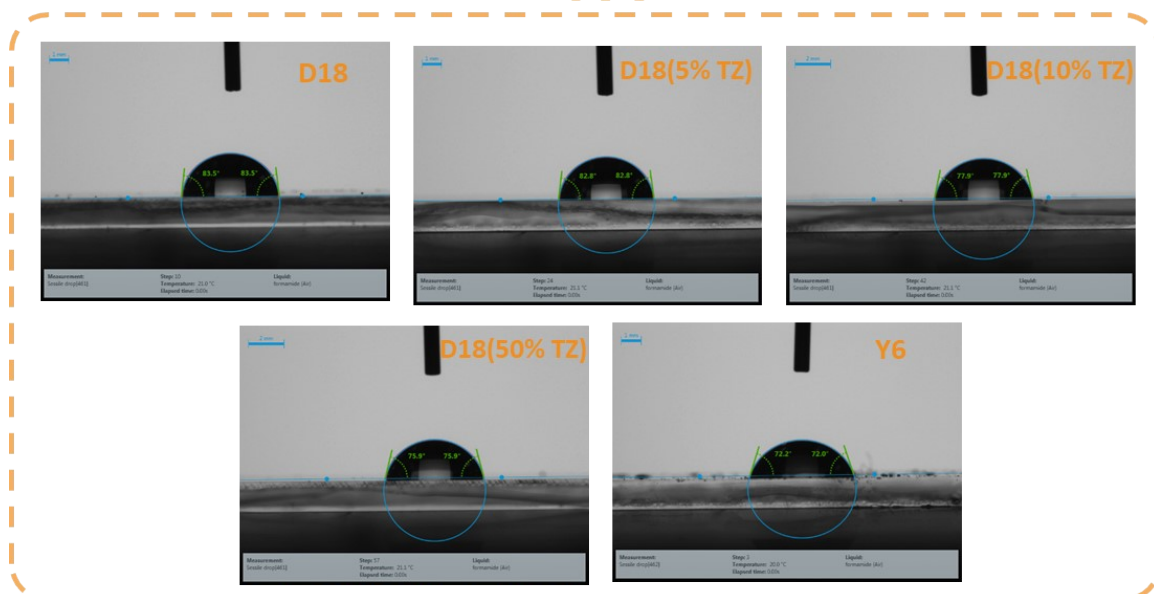| Blend	$\chi_{donor-acceptor}$[b] ($\times 10^{-2}$K)
D18:Y6	59.4
D18(5%TZ):Y6	50.2
D18(10%TZ):Y6	12.5
D18(50%TZ):Y6	1.3

H₂O

FA

Figure S20. The Deionized water and FA contact angles of the D18, D18(5% TZ), D18(10% TZ), D18(50% TZ), and Y6 pristine films.
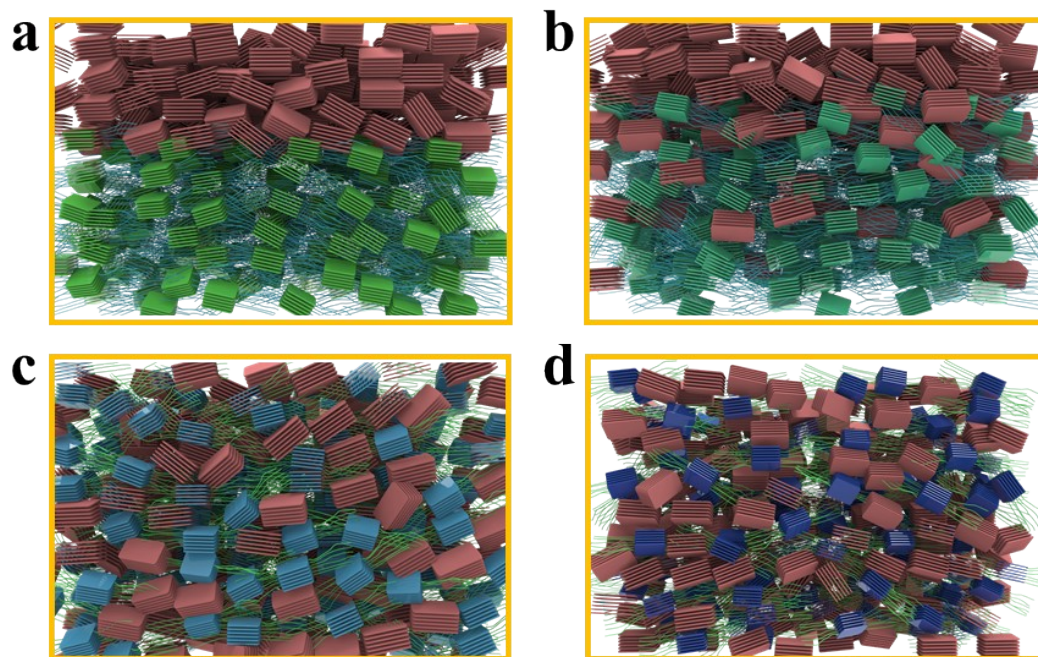
Figure S21. The D/A miscibility schematic drawing of **a** D18:Y6, **b** D18(5%TZ):Y6, **c** D18(10%TZ):Y6, and **d** D18(50%TZ):Y6 blend films.

19. Outdoor Stability Study

The D18-based terpolymer devices were first soldered with solar ribbons (Ulbrich Solar Technologies) to extend the device electrodes. The devices were then sandwitched between 2 layers of tempered glasses and 2 layers of encapsulants (Thermoplastic polyurethane). Butyl rubber edge sealant (PVS 101) is used to avoid moisture ingress from the side of the device. The stack is vacuum laminated in a laminator (Ecolam5 Ecoprogetti) at 120°C for 15mn. For outdoor stability measurement, the encapsulated devices were mounted at KAUST campus in a hot desert climate, with a tilt angle of 25°C and south-facing orientation. Devices were masked with a black tape, and J-V scans were performed approximately every 10 min during the daytime. The solar irradiance was recorded using a calibrated pyrometer (EKO MS-80). The devices were monitored under MPP tracking (TUV Rheinland). Every 10 mn, IV curves are recorded. Data acquisition was performed using EKO's MP160 software.

Figure S22. a The encapsulated D18-based terpolymer devices for outdoor stability test. **b-c** The photos of the outdoor stability test site in KAUST campus.

20. Hyperspectral PL

The encapsulated D18-based terpolymer devices before and after outdoor stressing were characterized using hyperspectral PL imaging system equipped with an optical microscope with a 20 × objective and a 532 nm laser.
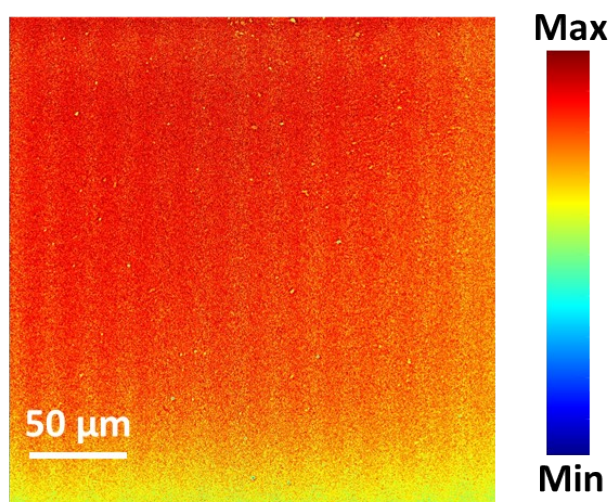

Figure S23. The illustration of the test area for hyperspectra PL characterization.
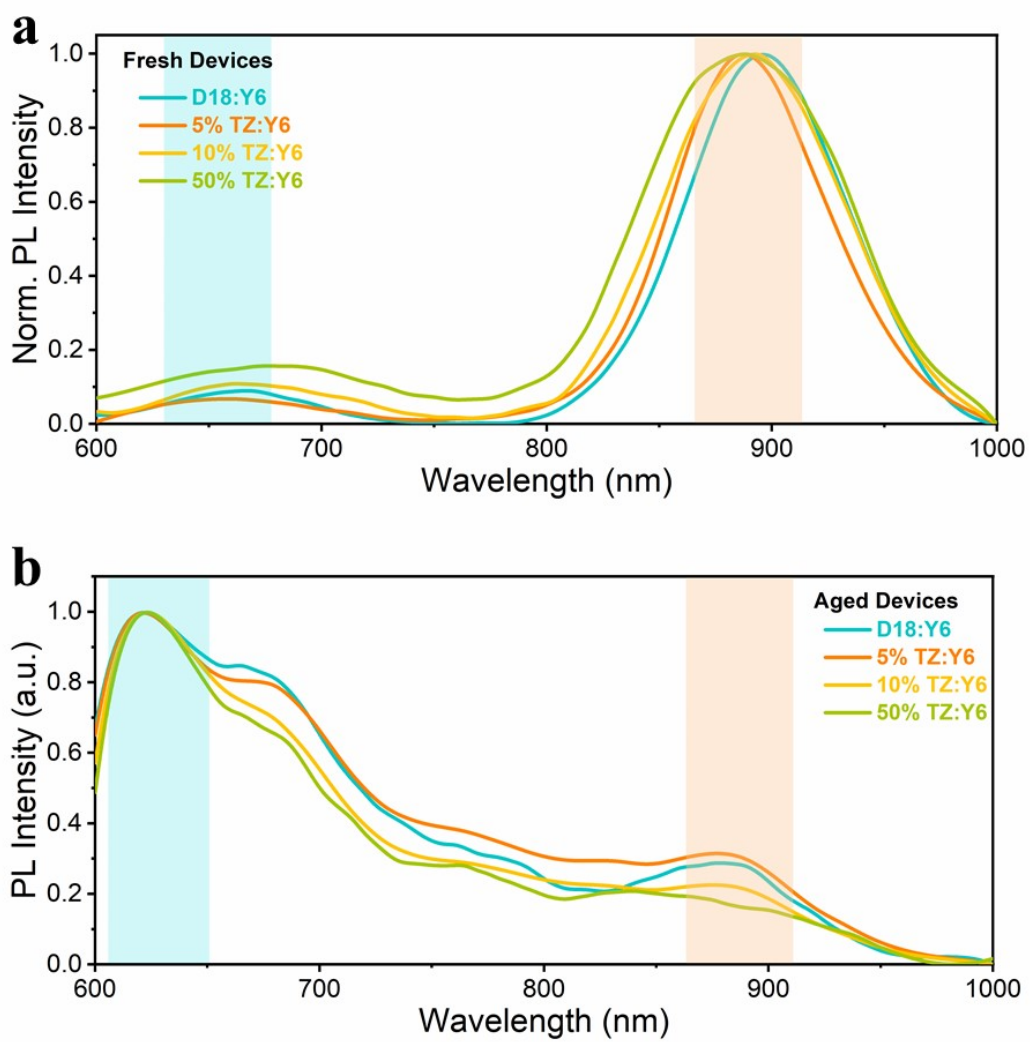
Figure S24. Normalized PL intensity of the corresponding mapping area of the **a** fresh and **b** aged devices.

21. Reference

1. M. Jeong, S. Chen, S. M. Lee, Z. Wang, Y. Yang, Z.-G. Zhang, C. Zhang, M. Xiao, Y. Li and C. Yang, *Adv. Energy Mater.*, 2018, **8**, 1702166.

2. X. Xu, K. Feng, Z. Bi, W. Ma, G. Zhang and Q. Peng, *Adv. Mater.*, 2019, **31**, 1901872.

3. H. Sun, T. Liu, J. Yu, T.-K. Lau, G. Zhang, Y. Zhang, M. Su, Y. Tang, R. Ma, B. Liu, J. Liang, K. Feng, X. Lu, X. Guo, F. Gao and H. Yan, *Energy Environ. Sci.*, 2019, **12**, 3328-3337.

4. T. Wang, R. Sun, M. Shi, F. Pan, Z. Hu, F. Huang, Y. Li and J. Min, *Adv. Energy Mater.*, 2020, **10**, 2000590.

5. J. Wu, G. Li, J. Fang, X. Guo, L. Zhu, B. Guo, Y. Wang, G. Zhang, L. Arunagiri, F. Liu, H. Yan, M. Zhang and Y. Li, *Nat. Commun.*, 2020, **11**, 4612.

6. X. Guo, Q. Fan, J. Wu, G. Li, Z. Peng, W. Su, J. Lin, L. Hou, Y. Qin, H. Ade, L. Ye, M. Zhang and Y. Li, *Angew. Chem. Int. Ed.*, 2021, **60**, 2322-2329.

7. R. Sun, T. Wang, Z. Luo, Z. Hu, F. Huang, C. Yang and J. Min, *Sol. RRL*, 2020, **4**, 2000156.

8. Y. Cheng, H. Jin, J. Oh, X. Huang, R. Lv, B. Huang, Z. Ma, C. Yang, L. Chen and Y. Chen, *J. Mater. Chem. A*, 2021, **9**, 9238-9247.

9. M. Jeong, J. Oh, Y. Cho, B. Lee, S. Jeong, S. M. Lee, S. H. Kang and C. Yang, *Adv. Funct. Mater.*, 2021, **31**, 2102371.

10. S. Chandrabose, K. Chen, A. J. Barker, J. J. Sutton, S. K. K. Prasad, J. Zhu, J. Zhou, K. C. Gordon, Z. Xie, X. Zhan and J. M. Hodgkiss, *J. Am. Chem. Soc.*, 2019, **141**, 6922-6929.

11. I. A. Howard, R. Mauer, M. Meister and F. Laquai, *Journal of the American Chemical Society*, 2010, **132**, 14866-14876.

12. S. Karuthedath, A. Melianas, Z. Kan, V. Pranculis, M. Wohlfahrt, J. I. Khan, J. Gorenflot, Y. Xia, O. Inganas, V. Gulbinas, M. Kemerink and F. Laquai, *Journal of Materials Chemistry A*, 2018, DOI: 10.1039/C8TA01692E.

13. S. Karuthedath, J. Gorenflot, A. Melianas, Z. Kan, M. Kemerink and F. Laquai, *The Journal of Physical Chemistry Letters*, 2020, **11**, 2838-2845.

14. J. Gorenflot, M. C. Heiber, A. Baumann, J. Lorrmann, M. Gunz, A. Kämpgen, V. Dyakonov and C. Deibel, *Journal of Applied Physics*, 2014, **115**, 144502.

15. F. Deledalle, P. Shakya Tuladhar, J. Nelson, J. R. Durrant and T. Kirchartz, *The Journal of Physical Chemistry C*, 2014, **118**, 8837-8842.

16. T. M. Burke, S. Sweetnam, K. Vandewal and M. D. McGehee, *Advanced Energy Materials*, 2015, **5**, 1500123.

17. S. Karuthedath, A. Melianas, Z. Kan, V. Pranculis, M. Wohlfahrt, J. I. Khan, J. Gorenflot, Y. Xia, O. Inganäs, V. Gulbinas, M. Kemerink and F. Laquai, *J. Mater. Chem. A*, 2018, **6**, 7428-7438.

18. J. Lv, H. Tang, J. Huang, C. Yan, K. Liu, Q. Yang, D. Hu, R. Singh, J. Lee, S. Lu, G. Li and Z. Kan, *Energy Environ. Sci.*, 2021, **14**, 3044-3052.

19. H. Tang, H. Chen, C. Yan, J. Huang, P. W. K. Fong, J. Lv, D. Hu, R. Singh, M. Kumar, Z. Xiao, Z. Kan, S. Lu and G. Li, *Adv. Energy Mater.*, 2020, **10**, 2001076.

20. M.-C. Michalski, J. Hardy and B. J. V. Saramago, *J. Colloid Interface Sci.*, 1998, **208**, 319-328.

21. D. K. Owens and R. C. Wendt, *J. Appl. Polym. Sci.*, 1969, **13**, 1741-1747.

22. Z. Cao, J. Chen, S. Liu, M. Qin, T. Jia, J. Zhao, Q. Li, L. Ying, Y.-P. Cai, X. Lu, F. Huang and Y. Cao, *Chem. Mater.*, 2019, **31**, 8533-8542.

23. S. Pang, R. Zhang, C. Duan, S. Zhang, X. Gu, X. Liu, F. Huang and Y. Cao, *Adv. Energy Mater.*, 2019, **9**, 1901740.